Monthly Notices
of the
ROYAL ASTRONOMICAL SOCIETY

MNRAS **449,** 1769–1781 (2015) doi:10.1093/mnras/stu2297

The JCMT Gould Belt Survey: constraints on prestellar core properties in Orion A North

C. J. Salji,[1,2]★ J. S. Richer,[1,2] J. V. Buckle,[1,2] J. Hatchell,[3] H. Kirk,[4] S. F. Beaulieu,[5] D. S. Berry,[6] H. Broekhoven-Fiene,[7] M. J. Currie,[6] M. Fich,[5] T. Jenness,[6,8] D. Johnstone,[4,6,7] J. C. Mottram,[9] D. Nutter,[10] K. Pattle,[11] J. E. Pineda,[12, 13]† C. Quinn,[10] S. Tisi,[5] S. Walker-Smith,[1,2] J. Di Francesco,[4,7] M. R. Hogerheijde,[9] D. Ward-Thompson,[11] P. Bastien,[14] H. Butner,[15] M. Chen,[7] A. Chrysostomou,[16] S. Coude,[14] C. J. Davis,[17] E. Drabek-Maunder,[18] A. Duarte-Cabral,[3] J. Fiege,[19] P. Friberg,[6] R. Friesen,[20] G. A. Fuller,[13] S. Graves,[1,2] J. Greaves,[21] J. Gregson,[22,23] W. Holland,[24,25] G. Joncas,[26] J. M. Kirk,[11] L. B. G. Knee,[4] S. Mairs,[7] K. Marsh,[10] B. C. Matthews,[4,7] G. Moriarty-Schieven,[4] J. Rawlings,[27] D. Robertson,[28] E. Rosolowsky,[29] D. Rumble,[3] S. Sadavoy,[30] H. Thomas,[6] N. Tothill,[31] S. Viti,[27] G. J. White,[22,23] C. D. Wilson,[28] J. Wouterloot,[6] J. Yates[27] and M. Zhu[32]

Affiliations are listed at the end of the paper

Accepted 2014 October 29. Received 2014 October 24; in original form 2014 July 15

ABSTRACT

We employ SCUBA-2 (Submillimetre Common-User Bolometer Array 2) observations of the Orion A North molecular cloud to derive column density and temperature maps. We apply a novel, Hessian-based structural identification algorithm for detection of prestellar cores to these data, allowing for automated generation of the prestellar mass function. The resulting mass function is observed to peak at $1.39^{+0.18}_{-0.19}$ $M_{\odot}$, indicating a star-forming efficiency lower limit of ∼14 per cent when compared with the Orion nebula Cluster initial mass function (IMF) peak. Additionally, the prestellar mass function is observed to decay with a high-mass power-law exponent $\alpha = 2.53^{+0.16}_{-0.14}$, indicating approximate functional similarity with the Salpeter IMF ($\alpha = 2.35$). This result, when combined with the results of previous investigations suggests a regional dependence of the star-forming efficiency.

Key words: stars: formation – stars: protostars – submillimetre: ISM.

1 INTRODUCTION

The development of large-scale, sub-mm surveys of nearby molecular clouds over recent decades have revealed thousands of compact sources believed to be the dusty condensations or 'cores' that precede star formation (Wynn-Williams 1982). The distribution of prestellar core masses has been observed to consistently mimic the form of the stellar initial mass function (IMF) shifted to higher masses by a factor of ∼3 (Nutter & Ward-Thompson 2007; Enoch et al. 2008; Könyves et al. 2010). This result suggests that stellar masses are determined at an early stage of fragmentation in the molecular cloud with a star-forming efficiency independent of core mass. The verification of such observations requires large-scale, deep sub-mm surveys of multiple, physically distinct regions with accurately calibrated temperature-corrected mass estimates using automated core identification algorithms. While the use of space-based sub-mm observatories such as *Herschel* provides large-scale maps with high sensitivity, in highly clustered regions the superior resolution of ground-based sub-mm observatories can reduce the potential mass overestimation effect due to apparent overlapping cores. This study presents the prestellar core mass function (CMF) in the Orion A North molecular cloud, derived using data observed on behalf of the James Clerk Maxwell Telescope (JCMT) Gould Belt Legacy Survey (GBS; Ward-Thompson et al. 2007).

1.1 The Gould Belt Survey

The GBS has been awarded 612 h of observation time with the JCMT to survey nearby star-forming regions (within 500 pc),

† E-mail: cs673@cam.ac.uk
Current address: Institute for Astronomy, ETH Zurich, Wolfgang-Pauli-Strasse 27, CH-8093 Zurich, Switzerland.

using HARP (Heterodyne Array Receiver Programme; Buckle et al. 2009) and SCUBA-2 (Submillimetre Common-User Bolometer Array 2; Holland et al. 2013). The SCUBA-2 component has observed and continues to observe the aforementioned molecular cloud regions at both 450 and 850 μm, tracing the emission of cold, high column density dust associated with the earliest stages of star formation. The simultaneous observing at 450 and 850 μm samples the dust spectral energy distribution, allowing one to estimate dust temperature and column densities for assumed dust emissivity β and opacity κ. The derivation of these physical properties allow us to address one of the key GBS science goals regarding the origin of the IMF.

1.2 Orion A North

This region (also known as the 'Integral-shaped filament') at ∼450 pc is one of the most active and well-studied sites of star formation near to the Sun (Johnstone & Bally 1999). The relative proximity and large number of young stellar objects (YSOs) contained within the cloud allows for enhanced mass sensitivity and statistical significance of physical quantities derived from observations. Additionally, a broad spectrum of physical environments are present within the region ranging from relatively quiescent gas to the violent outflows of OMC-1 (Johnstone & Bally 1999). Within such locations, relatively well established, universally observed relationships such as the nitial/core mass function may be more rigorously challenged. Distance estimates of Orion A vary considerably but the vast majority lie between 400–500 pc (Muench et al. 2008; Schlafly et al. 2014) and as a result, we adopt a distance of 450 pc.

1.3 Overview of SCUBA-2

SCUBA-2 is a 10 000 pixel bolometer camera capable of simultaneous observing at 450 and 850 μm. By taking advantage of superconducting transition edge sensor technology and the production of large-scale array structures, SCUBA-2 has been able to surpass its predecessor in overall mapping speed by factors of ∼100–150 (Holland et al. 2013). The 15 m diameter JCMT primary dish delivers angular resolutions of ∼ 8 arcsec and 13 arcsec at 450 and 850 μm, respectively, allowing for resolutions exceeding the *Herschel* Spectral and Photometric Imaging REceiver 500 μm instrument by a factor of >2.5.

2 OBSERVATIONS AND DATA REDUCTION

Between 2011 November and 2013 October, a total of 23, ∼ 40 min observations at 850 μm and 450 μm were made of fully sampled 30 and 15 arcmin diameter circular regions using PONG1800 and 900 mapping modes as described in Kackley et al. (2010). All observations of Orion A North were conducted during grade 1 or 2 weather defined according to the opacity at 225 GHz $\tau_{225} < 0.08$ and were made under Project IDs MJLSG22 and MJLSG31. The data were reduced using an iterative map-making technique (MAKEMAP; Chapin et al. 2013), and gridded to 1 arcsec pixels both at 850 and 450 μm. This super-Nyquist sampling is required for more accurate beam-matching (see Section 3.1) after which the maps are binned to approximately Nyquist sampling with a pixel size of 6 arcsec at both 450 and 850 μm. The iterations were halted when the map pixels, on average, changed by <0.1 per cent of the estimated map rms. The initial reductions of each individual scan were co-added to form a mosaic from which a signal-to-noise mask was produced.

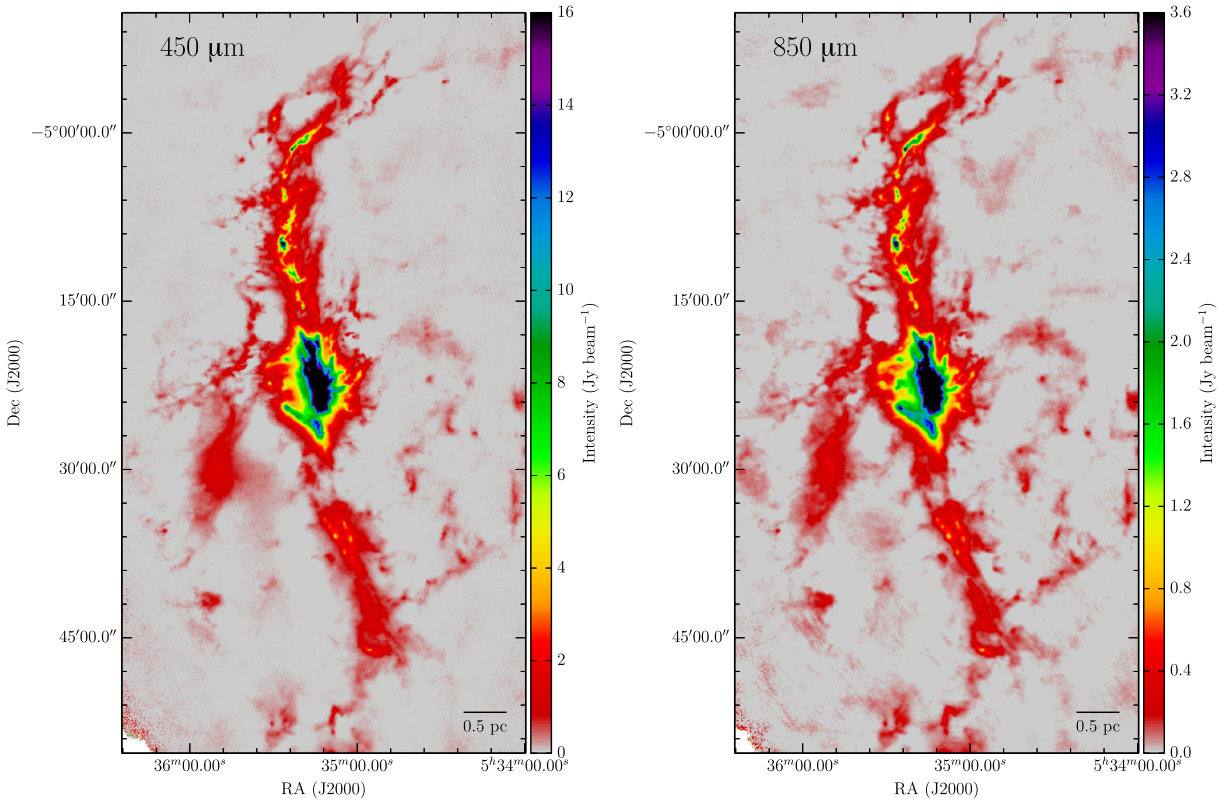

Figure 1. SCUBA-2 450 (left) and 850 μm (right) intensity mosaics at original resolutions of 8 arcsec and 13 arcsec, respectively (as specified in Section 1.3).

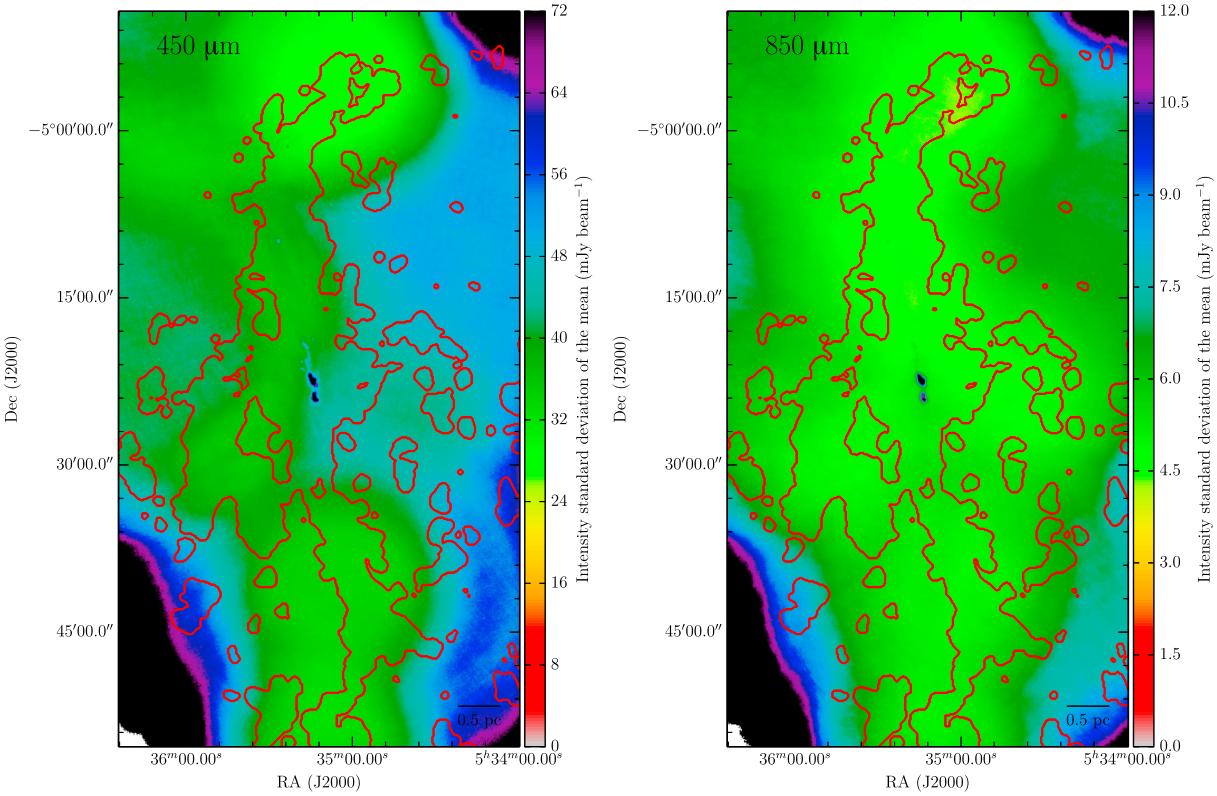

Figure 2. 1σ noise maps corresponding to the standard deviation of the mean of bolometer values that pass through each pixel. The red contour outlines the extent of the external mask – outside of which, the intensity measurements are deemed unreliable. The 450 μm noise map (left) displays more structure as the atmospheric opacity varies more strongly with the atmospheric precipitable water vapour than at 850 μm as shown in Fig. 3.

The final mosaics (shown in Fig. 1) were both produced from a second reduction using the 850 μm mask to define areas of emission as shown by the red contour in Fig. 2. It should be noted that the 850 μm mask was used to produce both the 450 and 850 μm mosaics as the 850 μm observations used to generate the mask are less prone to noise-based artefacts resulting from atmospheric fluctuations that are common in 450 μm observations.

Signals with temporal variation time-scales slower than 1.5 s were deemed to be atmospheric signal and were discarded during the post-observation, map-making process for both observing modes. This filtering results in an effective removal of all spatial frequencies below 0.67 Hz or structures with scales exceeding 600 arcsec. The presence of the two different mapping modes leads to non-uniform spatial sensitivity due to the differences in scan speed but also aids in increasing overall sensitivity. Flux recovery investigations were conducted on the PONG1800 mapping mode by analysing the output signal from fake Gaussian sources. The results of this analysis confirmed robust flux recovery for sources with a Gaussian FWHM <2.5 arcmin. The results of this investigation may be extended to the PONG900 mapping mode through the ratio of scan speeds for the two observing modes. The scan speeds for the PONG1800 and 900 observing modes are 400 and 280 arcsec s^{-1}, resulting in a theoretical robust signal recovery for sources with Gaussian FWHM <1.75 arcmin. This value corresponds to ∼0.23 pc, which is considered a few times larger than the average radii of prestellar cores (Foster et al. 2009) thus validating the combination of the two mapping modes into the final mosaics.

The data are calibrated in Jy $beam^{-1}$, using flux correction factors (FCFs) of 537 ± 26 and 491 ± 67 Jy pW^{-1} $beam^{-1}$ at 850 and 450 μm, respectively, derived from average values of JCMT calibrators (Dempsey et al. 2013). The PONG scan pattern leads to lower noise in the map centre and overlap regions, while data reduction and emission artefacts can lead to small variations in the noise over the whole map. The noise for each observation is given by the standard deviation of the mean of the bolometer signals that pass through each pixel averaged over the primary regions of emission, resulting in 1σ noise values at 450 and 850 μm of approximately 35 and 6 mJy $beam^{-1}$, respectively (see Fig. 2).

2.1 CO decontamination

Due to the strong ^{12}CO emission in molecular clouds, observations where the continuum filter profile overlaps with the frequency of such high-intensity lines produces contamination which must be removed to accurately estimate the continuum emission. While the majority of sources have a relatively low CO contamination < 20 per cent, regions with broad-line emission such as molecular outflows can contribute up to 79 per cent of observed emission through the SCUBA-2 850 μm filter (Drabek et al. 2012). The 450 and 850 μm SCUBA-2 filter profiles coincide with ^{12}CO $J = 6 \rightarrow 5$ and $J = 3 \rightarrow 2$ emission lines, respectively. However, the degree of possible CO contamination is dictated by the emission line location relative to the SCUBA-2 filter response. As can be seen from Fig. 3, the ^{12}CO $J = 3 \rightarrow 2$ line lies at the peak of the 850 μm filter response, while the $J = 6 \rightarrow 5$ line lies at a relatively low response value (approximately 50 per cent of the peak transmission) in the 450 μm filter profile. Unfortunately, we lack the ^{12}CO $J = 6 \rightarrow 5$ observations of Orion A North to decontaminate the 450 μm observations – however, if we consider the relatively low filter response for the $J = 6 \rightarrow 5$ transition and combine it with the ratio of energy level

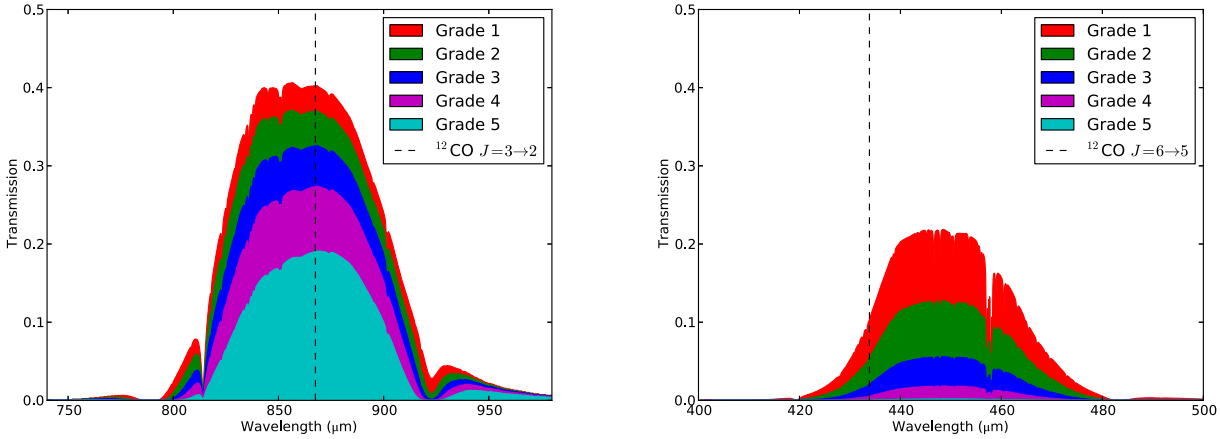

Figure 3. Left: combined atmospheric and 850 μm filter profile as a function of weather band – note that the ^{12}CO $J = 3 \rightarrow 2$ lies at a high response level. Right: equivalent plot for the 450 μm filter profile – note that the ^{12}CO $J = 6 \rightarrow 5$ lies at a relatively low response level.

populations – assuming a maximum CO excitation temperature of 30 K (in local thermodynamic equilibrium), the maximum contamination from the $J = 6 \rightarrow 5$ line will be ∼10 per cent of the $J = 3 \rightarrow 2$ line. In light of this, the decontamination process is applied only to the 850 μm data.

For ^{12}CO $J = 3 \rightarrow 2$ decontamination, we employ HARP observations reduced by Graves (2011). In order to mimic the spatial filtering of the SCUBA-2 data to correctly subtract the CO signal, the integrated ^{12}CO $J = 3 \rightarrow 2$ observation is converted to the raw units of SCUBA-2 observations (pW) and inserted as a negative source into the iterative map maker (Drabek et al. 2012). The factor required to convert between the integrated ^{12}CO $J = 3 \rightarrow 2$ and the continuum measurements of SCUBA-2 varies according to weather band since the filtered transmission intensity at the line frequency varies relative to the integrated filter profile. These conversion factors are derived in Drabek et al. (2012) and applied to each of the 23 observations according to the observed weather band prior to subtraction from the individual 850 μm continuum observations. The resulting ratio between the uncorrected continuum and ^{12}CO $J = 3 \rightarrow 2$ integrated intensity map indicates that the average contamination is of the order of ∼1–10 per cent, though in some regions reaching as high as 80 per cent (see Fig. 4). While some of these regions are spatially correlated with Herbig–Haro objects (Davis et al. 2009), some have no obvious outflow activity but appear to occur

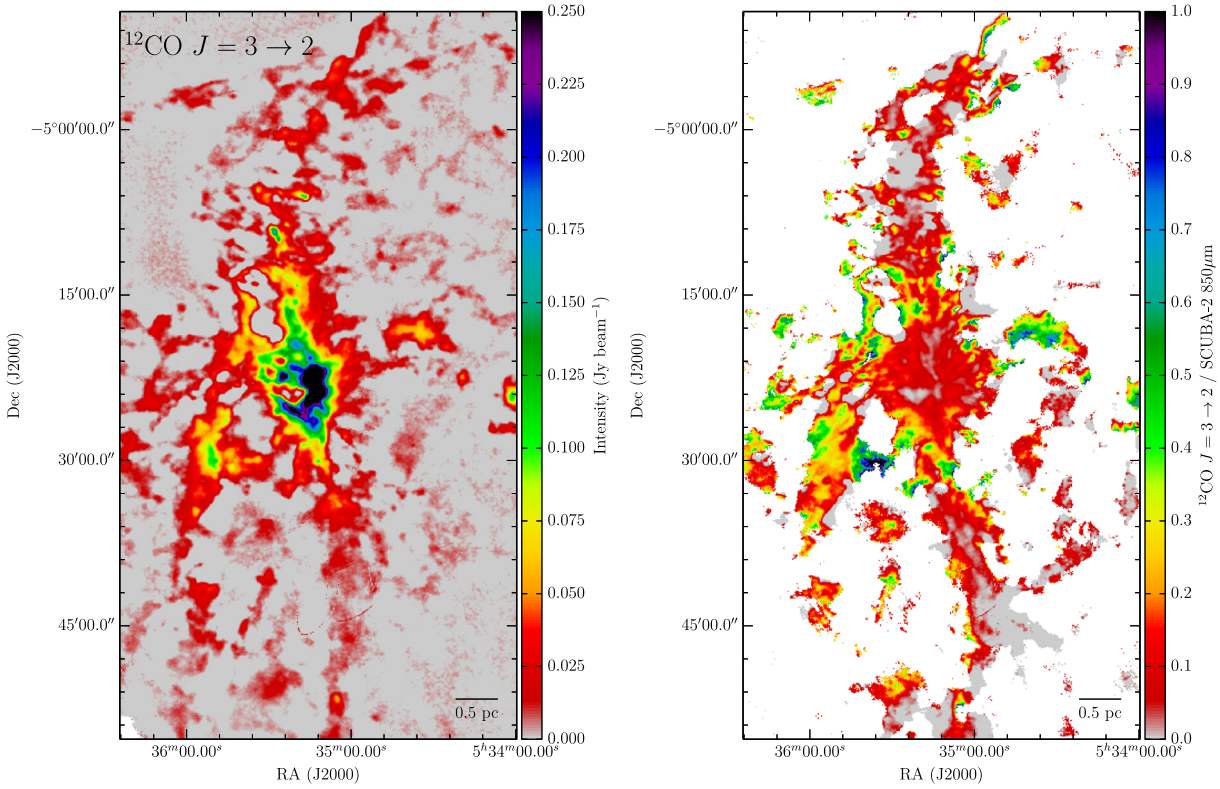

Figure 4. Left: HARP integrated ^{12}CO $J = 3 \rightarrow 2$ corrected for SCUBA-2 spatial filtering. Right: ratio map indicating the 850 μm contamination fraction – note that the majority of regions of high column density do not exceed 10 per cent contamination while some localized regions can reach as high as 90 per cent. Regions with 850 μm emission with signal-to-noise ratio ≤ 5 have been discarded and are shown as blank (white).

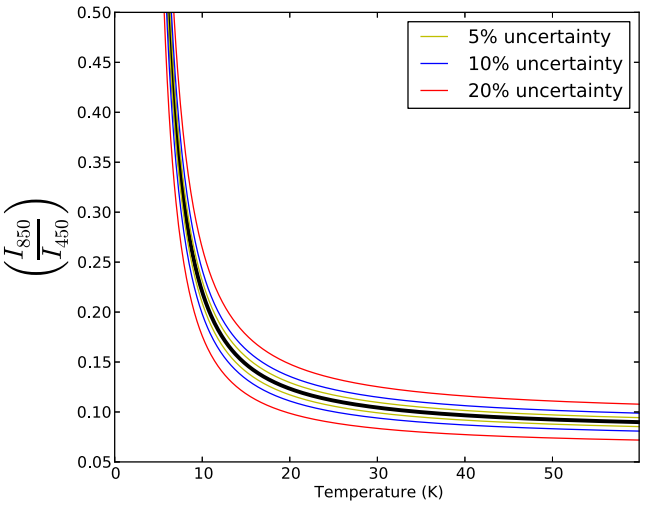

Figure 5. The variation of the intensity ratio as a function of dust temperature. The yellow, blue and red lines signify the effect of 5, 10 and 20 per cent uncertainties in the intensity ratio. The horizontal distance between the thick black curve and the coloured lines at a given temperature indicates the uncertainty in the temperature estimate. As the temperature increases towards ∼30 K, the Planck function approaches the Rayleigh–Jeans limit at 450 μm and temperature discrimination is lost. However, well below this temperature one can see that the 850 to 450 μm ratio strongly constrains dust temperatures (in the case of 5–10 per cent uncertainty).

within ∼15 arcmin of OMC-1 – possibly suggesting the presence of low column density regions of externally heated gas.

3 DUST COLUMN DENSITY AND TEMPERATURE ESTIMATION

The theoretical dust emission from an optically thin ($\tau \ll 1$) slab takes the form of a modified blackbody given by

$$I_\nu = \kappa_{\nu_0} \left(\frac{\nu}{\nu_0}\right)^\beta \Sigma\ B_\nu(T), \tag{1}$$

where I_ν, Σ, β and $B_\nu(T)$ are the intensity at a given frequency ν, column density (dust + gas), dust emissivity index and Planck function, respectively (Hildebrand 1983). The assumption of the optically thin regime is justified as follows, $\tau = \kappa\Sigma$ therefore, assuming a fixed emissivity index $\beta = 2$, the column densities required to give an optical depth $\tau = 1$ are 15 and 28 g cm^{-2} at 450 and 850 μm, respectively. We find that all regions – apart from OMC-1 – have $\Sigma < 15\,\mathrm{g\,cm^{-2}}$ thus validating the $\tau \ll 1$ criterion required for use of equation (1). The ratio of the 450 and 850 μm intensities is independent of column density and forms an implicit equation (equation 2) that can be solved to derive a temperature for an assumed dust emissivity index.

$$\frac{I_{850}}{I_{450}} = \left(\frac{\nu_{850}}{\nu_{450}}\right)^{3+\beta} \left(\frac{\mathrm{e}^{\frac{h\nu_{450}}{kT}} - 1}{\mathrm{e}^{\frac{h\nu_{850}}{kT}} - 1}\right). \tag{2}$$

It should be noted that the 450 and 850 μm ratio can only provide accurate temperature estimates for cold regions < 30K assuming the FCF uncertainties given previously (see Fig. 5). In this instance, we assume the dust emission to be optically thin ($\tau_\nu \ll 1$), fix the dust emissivity index at $\beta = 2$ and the dust + gas (assuming a dust to gas mass ratio of $\frac{1}{100}$) opacity at $\kappa_{\nu_0} = 0.1$ cm^2 g^{-1} where $\nu_0 = 1000$ GHz as used in previous studies of cold molecular cloud cores (Motte & André 2001; André et al. 2010). The resulting

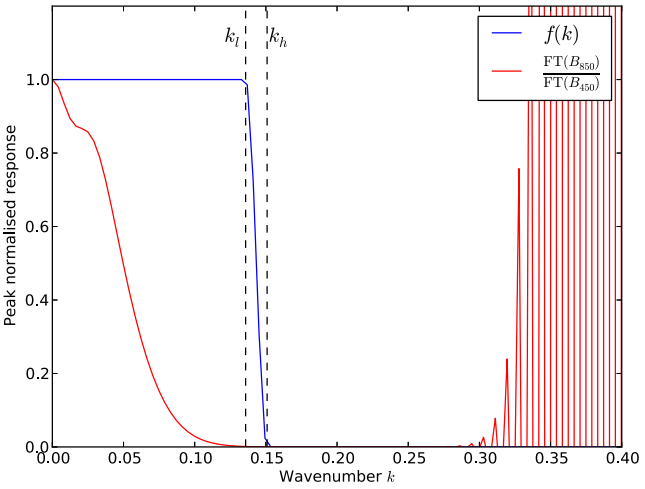

Figure 6. The one-dimensional slice through the filter response and peak normalized $\frac{\mathrm{FT}(B_{850})}{\mathrm{FT}(B_{450})}$. It is clear that the choice of k_h removes the contribution of high-frequency noise ($k > 0.3$) produced by division of extremely small values present in the Fourier transforms of the 450 and 850 μm beam profiles.

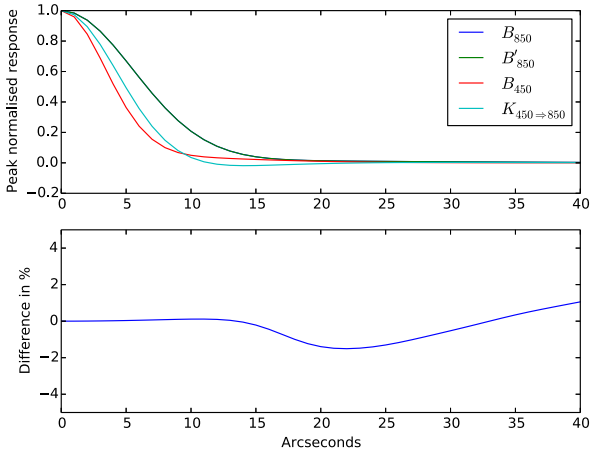

Figure 7. Top: one-dimensional slices through the beam models and kernel, note that the true 850 μm beam profile cannot be seen as it is perfectly overlapped by the reconstructed beam. Bottom: the percentage difference between the reconstructed and true 850 μm beam profiles $100 \times (\frac{B_{850}}{B'_{850}} - 1)$.

temperature estimate can be fed back into equation (1), to derive a column density estimate. However, to conduct a pixel by pixel estimation of the aforementioned physical properties, the intensity maps at 450 and 850 μm must have the same spatial resolution.

3.1 Common resolution beam convolution

While the SCUBA-2 beam profiles have relatively Gaussian profiles, they also exhibit a broad 'error' beam arising from panel-to-panel misalignment relative to an ideal parabola which contributes a considerable proportion of the integrated response (table 1 in Dempsey et al. 2013). A viable option to attain a common beam resolution between the 450 and 850 μm maps would be to convolve the 450 μm map with the 850 μm beam model and vice-versa (Reid & Wilson 2005; Hatchell et al. 2013). However, this option – while more straightforward – causes unnecessary loss of spatial

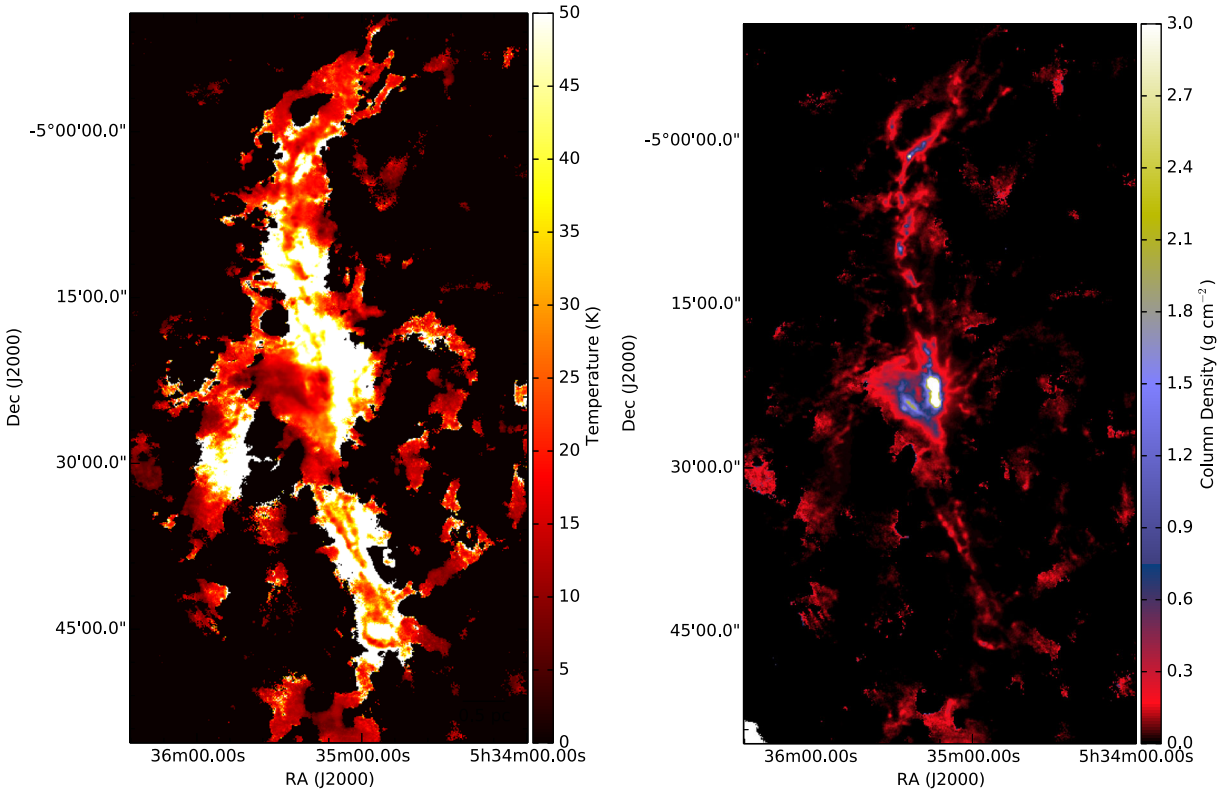

Figure 8. Left: dust temperature map derived from the 450 to 850 μm intensity ratio. Note that temperature estimates exceeding 50 K and areas where either the 450 or 850 μm signal drop below 5σ are coloured black. Right: dust column density map – note that all regions with corresponding temperature estimates exceeding 50 K are capped at this value due to large uncertainty as shown in Fig. 5.

resolution. Alternatively, one may generate a kernel $K_{A\Rightarrow B}$ which satisfies

$$B_B = K_{A\Rightarrow B} * B_A, \tag{3}$$

and is derived using

$$K_{A\Rightarrow B} = \mathrm{FT}^{-1}\left[\frac{\mathrm{FT}(B_B)}{\mathrm{FT}(B_A)}\right], \tag{4}$$

(where FT denotes the Fourier transform operator) avoiding unnecessary loss of spatial resolution. Additionally, we enforce an area-normalization of $\int K_{A\Rightarrow B}\,\mathrm{d}x = 1$ to ensure that the convolution process conserves total flux. While this deconvolution is mathematically simple, in practise the process requires filtering of the high-frequency components to avoid division by zero errors (Aniano et al. 2011). With the inclusion of the high-frequency filter, equation (4) becomes

$$K_{450\Rightarrow 850} = \mathrm{FT}^{-1}\left[\frac{\mathrm{FT}(B_{850})f(k)}{\mathrm{FT}(B_{450})}\right], \tag{5}$$

where B_{450} and B_{850} denote the 450 and 850 μm beam models (table 1 in Dempsey et al. 2013). The filter $f(k)$ takes the form of

$$f(k) = \begin{cases} 1, & \text{if } k < k_l \\ \frac{1}{2}\left[1+\cos\left(\pi + \frac{k-k_l}{k_h-k_l}\right)\right] & \text{if } k_l < k < k_h \\ 0, & \text{if } k > k_h \end{cases} \tag{6}$$

and is graphically represented in Fig. 6. All calculations were conducted on a 2048 × 2048 grid (in order to accelerate the fast fourier transform operation), representing a region of 140 arcsec × 140 arcsec. The value of k_h is defined as the wavenumber at which FT(B_{850}) separates the high-frequency noise from the low-frequency data (∼0.15 wavenumbers ≡ 3 arcsec – see Fig. 6) while $k_l = 0.9k_h$. The final choice of these values and filter function for $k_l < k < k_h$ were selected in order to maximize the accuracy of the beam reconstruction. The resulting reconstructed 850 μm beam profile B'_{850} accurately traces the true profile to within ∼1 per cent (see Fig. 7).With the accurately calibrated 450 and 850 μm measurements shifted to a common beam resolution, the ratio of intensities can be used to solve equation (2) via look-up table to determine the dust temperature. Only regions with emission exceeding the detector thermal noise by a factor of 5 at both 450 and 850 μm are considered. The derived temperature is then inserted into equation (1) to solve for the dust column density. The uncertainty in temperature estimation arises from an uncertainty in the intensity ratio as demonstrated in Fig. 5. The uncertainty in intensity has two components; the first and largest contributor is the uncertainty in flux conversion factor for which we assume values of 5 and 10 per cent at 850 and 450 μm, respectively (Dempsey et al. 2013); the second component arises due to the variation in bolometer signal that passes through each pixel. This two component uncertainty is used to derive a maximum and minimum intensity ratio estimate which translates directly through equations (2) and (1) to maximum and minimum temperature and column density estimates. The resulting maps are given in Fig. 8.

4 RESULTS

The results of numerous past studies indicate a functional similarity between the prestellar CMF and the IMF (Nutter & Ward-Thompson 2007; Enoch et al. 2008; André et al. 2010). Such observations provide an attractively simplistic theory of star formation where cores

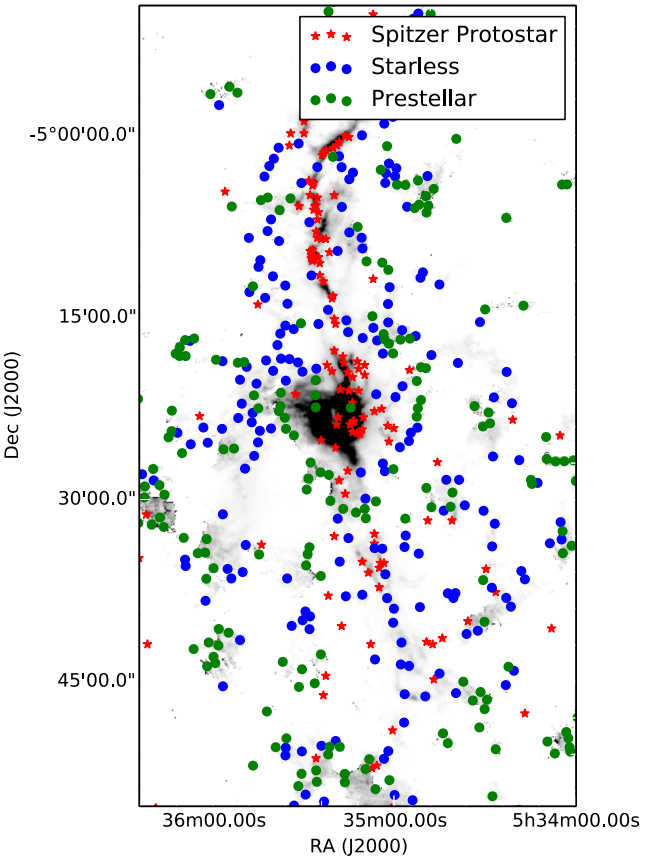

Figure 9. Greyscale column density map overlaid with markers indicating the locations of prestellar and starless core populations. The red star markers indicate protostellar sources as defined by the *Spitzer* survey of Orion A and B Molecular Clouds YSOs Catalog (Megeath et al. 2012)

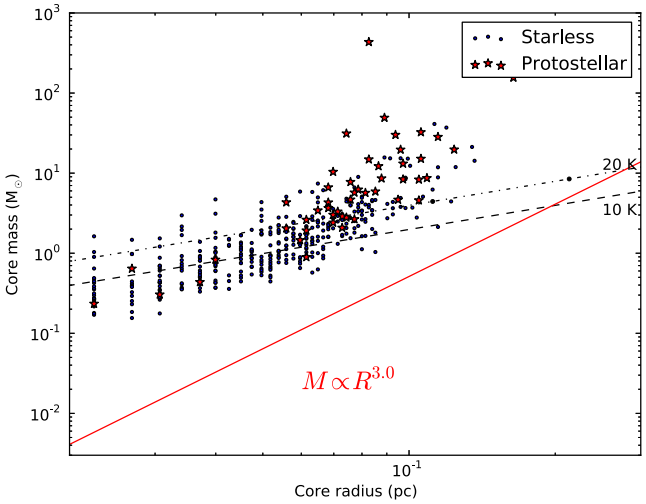

Figure 10. Scatter plot giving the distribution of core masses and radii. The dashed lines indicate $M_{\rm BE}$ assuming core temperatures of 10 and 20 K. Additionally, the theoretical mass–radius Larson law for a core population with constant internal thermal pressure and a constant kinetic temperature is shown in red (Lada et al. 2008).

simply convert mass to stars with a defined efficiency factor equal to the ratio of turnover points for the core and IMF. However, to confirm the universality of these observations requires large-scale, deep sub-mm surveys of multiple, physically distinct regions with temperature-corrected mass estimates and preferably automated core identification algorithms. In this study, we employ a highly customizable PYTHON implementation of a multiscale, Hessian-based, morphological identification algorithm capable of identifying both compact (see Appendix A) and elongated structures (Salji, Buckle & Richer, in preparation). Previous works that use similar techniques such as Molinari et al. (2011) and Schisano et al. (2014) limit their analysis to a single spatial scale. Additionally, after determining the second-order derivatives there is no exploitation of the structural information stored within the Hessian. In contrast, we apply a Hessian determinant filter (which preferentially detects radially symmetric sources) at a *variety* of spatial scales. We set the algorithm scale sensitivity to detect approximately circular cores with spatial scales ranging between 0.03–0.1 pc in accordance with previous studies (Foster et al. 2009) where the minimum scale is set by the beamwidth equivalent arc-length at 450 pc. A user-defined threshold is applied to the Hessian determinant map of 1×10^{-5} followed by a standardized algorithmic separation (Verveer 2003–2005) to label the cores (see Fig. 9). The diffuse background surrounding the core is estimated and subtracted by linearly interpolating the background in four directions across a masked region defined by the core boundaries in a similar manner to Men'shchikov et al. (2012). Each core mass was corrected to account for the ∼90 per cent mass recovery within the detected core boundary (see Appendix A). In addition to this, only cores with mass estimates exceeding the mass uncertainty by a factor of 3 were considered for further analysis. The cores were classified according to the presence or absence of at least one protostellar source as defined by the *Spitzer* survey of Orion A and B Molecular Clouds YSOs Catalog (Megeath et al. 2012) and the core boundaries shown in Fig. 9. Additionally, cores with a projected area smaller than the 850 μm beam were discarded as non-detections. The remaining cores comprised of 432 starless and 48 with at least one Spitzer protostellar source present within the clump boundaries. In order to determine which cores were to be considered 'prestellar', we combine measurements of core mass, radius and temperature and relate them through Bonnor–Ebert sphere (Bonnor 1956) criticality defined as

$$M_{\rm BE} = \frac{2.4 r k_{\rm B} T}{\mu m_{\rm p} G}, \tag{7}$$

where the variables r and T are the deconvolved core radius and temperature while $m_{\rm p}$, $k_{\rm B}$ and G denote the proton mass, Boltzmann and gravitational constants, respectively. The temperature is a simple average over the area defined by the core boundaries shown in Fig. 9. The deconvolved radius in this instance is estimated assuming that the core boundary is well approximated by a circle, that the core emission is approximately Gaussian and that the convolved radius is equivalent to the standard deviation σ of the core. This assumption allows for simple derivation of the deconvolved radius through quadrature subtraction of the unconvolved and beam radii. The assumption of approximate circularity is validated through the preferential detection of circular objects due to the determinant nature of the Hessian-based filtering (see Appendix A). The mean molecular mass $\mu = 2.33$ – is assumed to be consistent with a 3:1 hydrogen:helium abundance (by mass) ratio. Cores with masses exceeding $M_{\rm BE}$ are considered 'prestellar' (see Fig. 10). Of the 432 starless cores, 222 were considered to be subcritical with respect to $M_{\rm BE}$, leaving a total of 210 prestellar cores. Aside from a small number of extremely high mass cores, the vast majority of core masses lie within a few multiples of $M_{\rm BE}$ suggesting an approximately virialized core contraction. A catalogue containing

Table 1. A sample of prestellar cores and their properties (full catalogue available online).

Core ID	RA (J2000.0)	DEC (J2000.0)	Mass ($M_\odot$)	Temperature[a] (K)	Deconvolved radius (pc)
1	83.8756	−6.0257	7.4 ± 0.3	9.9 ± 2.3	0.06
2	83.7795	−6.0200	2.3 ± 0.3	10.4 ± 3.3	0.07
3	83.7621	−6.0161	2.5 ± 0.6	7.9 ± 0.7	0.06
4	83.7305	−6.0052	20.2 ± 2.7	5.9 ± 0.8	0.12
5	83.7574	−5.9980	2.5 ± 0.7	8.5 ± 0.7	0.08
6	83.9263	−5.9891	5.8 ± 0.9	5.4 ± 1.1	0.06
7	83.7278	−5.9772	41.1 ± 1.9	6.0 ± 1.1	0.11
8	83.7736	−5.9788	1.3 ± 0.3	13.0 ± 1.3	0.05
9	83.8850	−5.9584	3.7 ± 0.3	8.4 ± 1.7	0.10
10	83.6986	−5.9659	0.6 ± 0.2	5.0 ± 0.3	0.02
...	...	...	...	...	...
210	83.8666	−4.8046	0.3 ± 0.1	7.7 ± 0.6	0.01

Note. [a]Uncertainty is the standard deviation of temperature values within the core boundary.

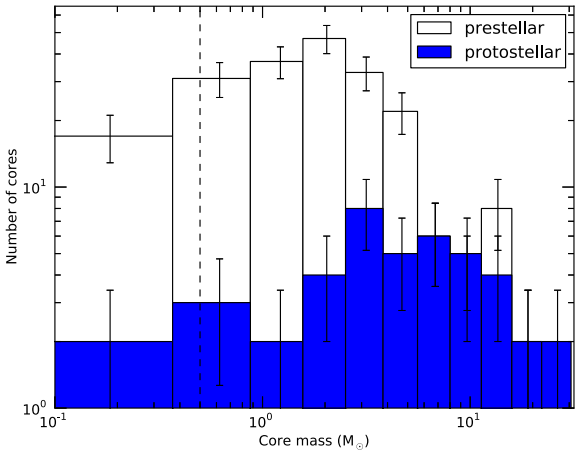

Figure 11. Temperature-corrected mass functions of protostellar and prestellar cores in Orion A North. The turnover point occurs around 1.4 $M_\odot$ for the prestellar cores, while the small population of protostellar cores has a poorly defined turnover. The vertical dotted line indicates the core mass detection and completeness limits of 0.5 $M_\odot$. The error bars shown are Poisson 'counting' errors, i.e $\sqrt{N}$.

the full core population properties is available in electronic format alongside this publication. A small sample of cores from this catalogue is presented in Table 1. The temperature-corrected prestellar and protostellar CMF are shown in Fig. 11. The completeness limit is of great concern when generating mass functions. This value relies predominantly on the ability of the source extraction algorithm to detect the full population of cores without distorting the derived mass function. Simulations of SCUBA-2 450 and 850 μm core recovery resulted in >85 per cent completeness for masses exceeding 0.5 $M_\odot$, the details of which are discussed in Appendix B. While the detection and completion limits are larger than the previous SCUBA study conducted by Nutter & Ward-Thompson (2007), the addition of temperature-corrected masses and automated source detection provide valuable and unbiased information regarding the form of the mass function. The importance of temperature-corrected masses is highlighted if one notes that for a constant intensity value, the difference in column density (and ultimately mass) for assumed isothermal temperatures of 10 and 20 K will differ by a factor of ∼3 resulting in the possibility of considerable distortions to the mass function.

To draw well-informed conclusions from the prestellar mass function, we employ the PYTHON-based, Markov Chain Monte Carlo, Bayesian analysis package PYMC (Patil, Huard & Fonnesbeck 2010) to sample the posterior probability distributions. A deterministic, lognormal probability density function model of the form

$$N(M) = \frac{K}{\sigma\sqrt{2\pi}M}\exp\left(-\frac{(\ln(M)-\mu)^2}{2\sigma^2}\right) \quad (8)$$

was employed to accurately locate the mass turnover point defined according to the mode of the distribution $\equiv e^{\mu-\sigma^2}$. For masses exceeding the completeness limit of 0.5 $M_\odot$, uniform priors of 0–1000, 0–10 and 0–2 were assumed for the free parameters K, μ and σ, respectively. The resulting posterior distribution of the mass function modal values (Fig. 13) yields a turnover point located at $1.39^{+0.18}_{-0.19}$ $M_\odot$, which exceeds the completeness limit by a factor >2. The high-mass tail of the CMF is fitted with a power law of the form $\frac{dN}{dlog(M)} = \frac{dN}{dM}M \propto M^{1-\alpha}$ for masses exceeding 2 $M_\odot$. A uniform prior of $\alpha = 0$–10 was assumed since the use of previous results of α obtained from past investigations (often with the undesirable isothermal approximation) would require one to assume that α does not vary with local environment – a postulate yet to be proven. Both posterior distributions were generated via Metropolis–Hastings steps and were each sampled a total of 500 000 times with the first 10 000 discarded as burn-in. The α posterior values and corresponding fits are shown in Figs 12 and 13 indicating $\alpha = 2.53^{+0.16}_{-0.14}$, a value which lies in accordance with the Salpeter IMF $\alpha = 2.35$ for $M \geq 1$ $M_\odot$ (Salpeter 1955). The characteristic mass found at $1.39^{+0.18}_{-0.19}$ $M_\odot$ is highly consistent with the result of Nutter & Ward-Thompson (2007), who observed a turnover at ∼1.3 $M_\odot$ and when compared with the stellar IMF characteristic mass of 0.2 $M_\odot$ for the Orion nebula Cluster (Hillenbrand 1997) yields a minimum star-forming efficiency $f_{SFE} \sim 0.14$ (this value will be increased by factor n assuming one core goes on to form n stars – independent of core mass – with no continued mass accretion during the protostellar phase). The remaining ground-based derivations of the prestellar CMF peak at ∼1 $M_\odot$ though all of these studies have assumed a single core temperature due to their lack of multifilter observations. Fig. 14 demonstrates the variety of prestellar core temperatures which can lead to considerable errors in absolute mass estimation for an assumed single temperature.

5 DISCUSSION

The majority of previous studies regarding prestellar mass functions have resulted in mass turnovers of ≈1 $M_\odot$ with Salpeter-like power laws, suggesting that the functional form of the IMF is defined during prestellar core formation (Nutter & Ward-Thompson 2007;

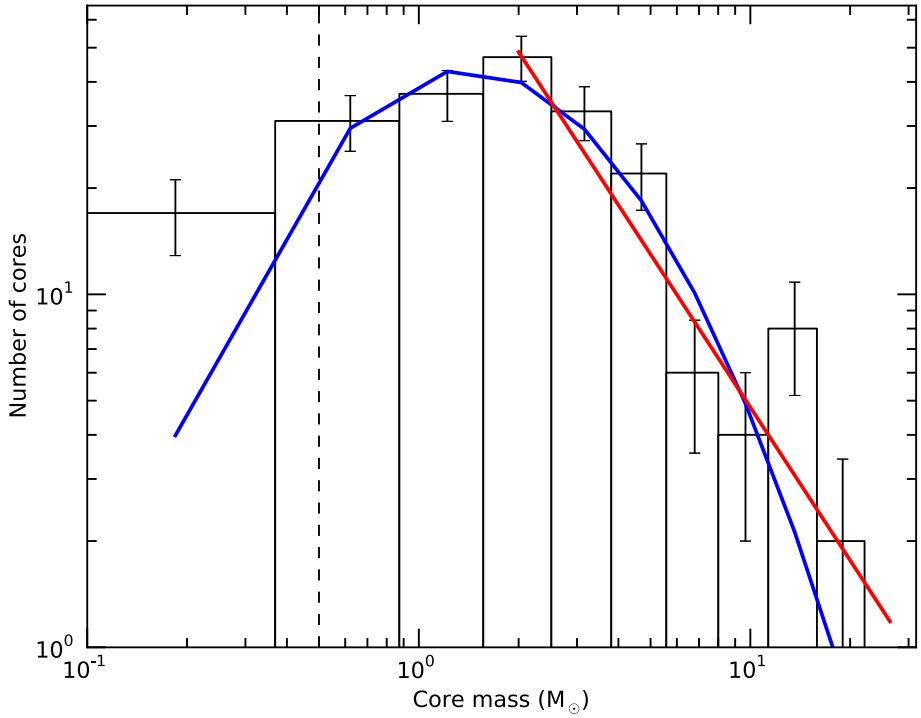

Figure 12. The prestellar CMF with a lognormal (blue) and Salpeter-like power law (red) at higher masses. The lognormal distribution modal value occurs at $1.39^{+0.18}_{-0.19}$ $M_\odot$, while the power-law posterior distribution peaks at $\alpha = 2.53^{+0.16}_{-0.14}$. The vertical dotted line indicates the core mass detection and completeness limits of 0.5 $M_\odot$.

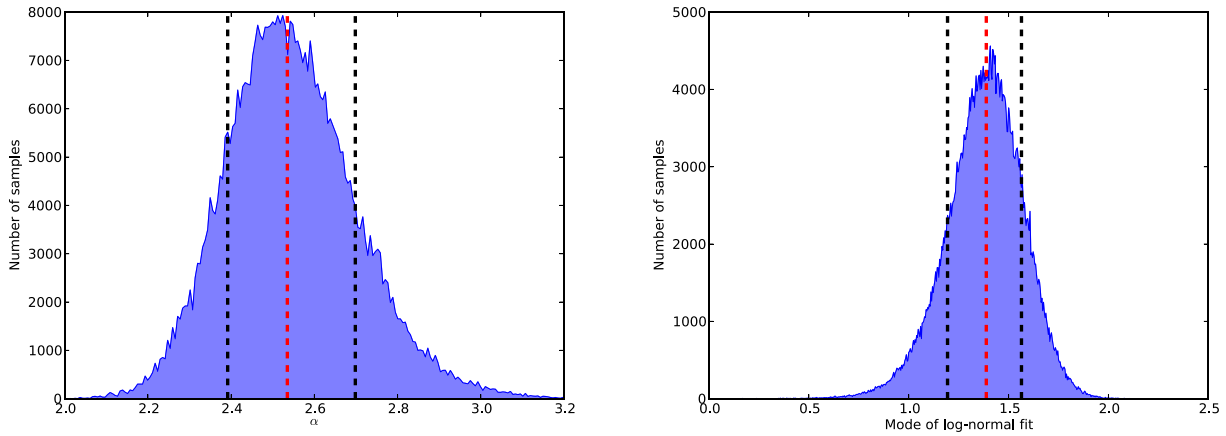

Figure 13. Left: posterior distribution of α for the prestellar core population with binning intervals of 0.006 and a total of 500 000 samples. Right: posterior distribution of the prestellar turnover mass value with binning intervals of 0.006 and (once again) 500 000 samples. The distribution exhibits greater noise structure as the mass peak is defined using two fitted parameters of the lognormal distribution each with their own approximately Gaussian posterior distribution. The dotted black and red lines indicate the median and 1σ boundaries, respectively.

Enoch et al. 2008; Könyves et al. 2010). The simplest explanation of these measurements suggests that each core goes on to form *n* stars with an efficiency that is *independent* of the core mass. Dunham et al. (2010) describe an accretion/mass-loss model where a fraction of the material accreted on to the young star is ejected in the form of a jet which transfers momentum to the envelope material resulting in considerable loss of mass to the core as a whole. The outflow cavity then reduces the solid angle of available gas to accrete from the envelope thus reducing the accretion rate with the collapse terminating when the conical outflow opening angle reaches 180°. The resulting star-forming efficiency $f_{\rm SFE}$ – defined as the fraction of initial core mass to the mass that is transferred to the star – yields values of $f_{\rm SFE} = 0.48$, 0.33 and 0.31 for initial core masses of 0.3, 1 and 3 $M_\odot$. While $f_{\rm SFE}$ has some dependence on mass, this only appears to occur for the low-mass core while $f_{\rm SFE}$ for core masses exceeding 1 $M_\odot$ have a weaker dependence which lies in accordance with the IMF mirrored CMF. However, while the absolute values of $f_{\rm SFE}$ derived in Dunham et al. (2010, using average jet/outflow parameters) differ from our estimate, it should be noted that these theorized values vary according to jet/outflow properties which are region-dependent quantities in addition to the uncertainty of how many stars are formed from each core which will increase

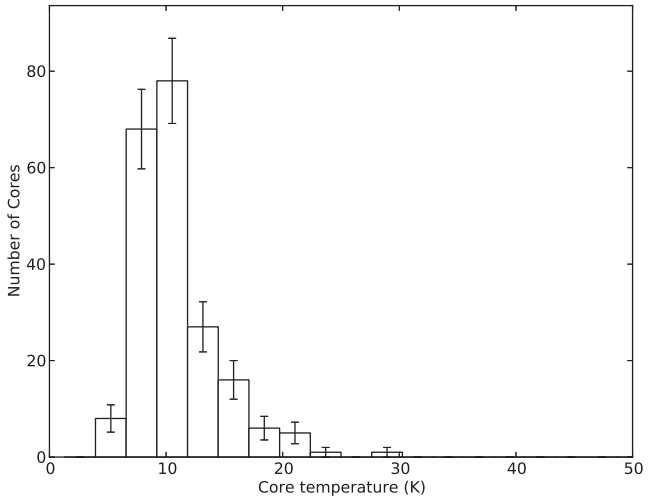

Figure 14. Histogram of prestellar core average temperatures. Note the spread in values which will lead to erroneous mass estimates for a single assumed temperature.

our estimate by the factor n. While the $f_{\rm SFE}$ mass independence at high masses is a promising result, further investigation involving in-depth outflow analysis is required to assess the validity of the Dunham et al. (2010) model.

A recent study of prestellar cores in Orion A South (also known as L1641) using temperature-corrected mass estimates derived a mass function with a characteristic mass located at 2.20 ± 0.05 M$_\odot$ defined by the superposition of two distinct mass functions peaking at 4 and 0.8 M$_\odot$ for prestellar cores located inside and outside of dusty filaments, respectively (Polychroni et al. 2013). This seemingly strong dependence of $f_{\rm SFE}$ on environment requires extensive follow-up investigations to deduce the cloud properties which may affect the value of $f_{\rm SFE}$.

In addition to physical properties of the host molecular cloud affecting the observed $f_{\rm SFE}$, the limited resolving power of the telescope can result in an overestimation of core masses as one cannot resolve multiple cores that lie within one beam area. This affect is demonstrated through the work of Takahashi et al. (2013) in which high-resolution Submillimetre Array (SMA) observations of OMC 2 and 3 detect 12 sources where SCUBA-2 can only resolve 5 or 6. If one assumes undercounting by this factor, the observed $f_{\rm SFE}$ will effectively double, resulting in a $f_{\rm SFE} \sim 0.29$ which lies in close accordance with the work of Dunham et al. (2010) mentioned above.

6 CONCLUSIONS

(i) We have successfully developed and applied a novel, Hessian-based, structural identification algorithm to column density and temperature estimation maps of the Orion A North molecular cloud. These maps were generated using advanced convolution kernel techniques, which allowed for the removal of unnecessary loss of spatial resolution.

(ii) The Bonnor–Ebert supercritical (prestellar) CMF was generated and observed to turnover at $1.39^{+0.18}_{-0.19}$ M$_\odot$, indicating a regional star-forming efficiency $f_{\rm SFE} = 0.14$. When compared with companion studies, our result suggests that $f_{\rm SFE}$ has some regional dependence.

(iii) A power-law model fit was applied to the masses exceeding the derived turnover mass and resulted in $\alpha = 2.53^{+0.16}_{-0.14}$, which lies in approximate accordance with the $\alpha = 2.35$ Salpeter IMF slope (Salpeter 1955).

The techniques outlined in this study provide a robust, automated method of generating prestellar and protostellar (temperature-corrected) mass functions using SCUBA-2 data. Applying these techniques to other Gould Belt molecular clouds at a variety of distances will provide larger samples to strengthen the statistical evidence regarding the high-mass Salpeter-like slope, characteristic mass and ultimately the variation of $f_{\rm SFE}$ with molecular cloud properties.

ACKNOWLEDGEMENTS

The James Clerk Maxwell Telescope is operated by the Joint Astronomy Centre on behalf of the Science and Technology Facilities Council of the United Kingdom, the National Research Council of Canada, and (until 31 March 2013) the Netherlands Organization for Scientific Research.

Additional funds for the construction of SCUBA-2 were provided by the Canada Foundation for Innovation.

This research used the facilities of the Canadian Astronomy Data Centre operated by the National Research Council of Canada with the support of the Canadian Space Agency.

REFERENCES

André P. et al., 2010, A&A, 518, L102
Aniano G., Draine B. T., Gordon K. D., Sandstrom K., 2011, PASP, 123, 1218
Bonnor W. B., 1956, MNRAS, 116, 351
Buckle J. V. et al., 2009, MNRAS, 399, 1026
Chapin E. L., Berry D. S., Gibb A. G., Jenness T., Scott D., Tilanus R. P. J., Economou F., Holland W. S., 2013, MNRAS, 430, 2545
Davis C. J. et al., 2009, A&A, 496, 153
Dempsey J. T. et al., 2013, MNRAS, 430, 2534
Drabek E. et al., 2012, MNRAS, 426, 23
Dunham M. M., Evans N. J., II, Terebey S., Dullemond C. P., Young C. H., 2010, ApJ, 710, 470
Enoch M. L., Evans N. J., II, Sargent A. I., Glenn J., Rosolowsky E., Myers P., 2008, ApJ, 684, 1240
Foster J. B., Rosolowsky E. W., Kauffmann J., Pineda J. E., Borkin M. A., Caselli P., Myers P. C., Goodman A. A., 2009, ApJ, 696, 298
Frangi R. F., Frangi R. F., Niessen W. J., Vincken K. L., Viergever M. A., 1998, in Wells W. M., Colchester A., Delp S. L., eds, Lecture Notes in Computer Science, Vol. 1496, Medical Image Computing and Computer-Assisted Interventation. Springer-Verlag, Berlin, p. 130
Graves S., 2011, PhD thesis, Univ. Cambridge
Hatchell J. et al., 2013, MNRAS, 429, L10
Hildebrand R. H., 1983, QJRAS, 24, 267
Hillenbrand L. A., 1997, AJ, 113, 1733
Holland W. S. et al., 2013, MNRAS, 430, 2513
Johnstone D., Bally J., 1999, ApJ, 510, L49
Kackley R., Scott D., Chapin E., Friberg P., 2010, in Radziwill N. M., Bridger A., Proc. SPIE Conf. Ser. Vol. 7740, Software and Cyberinfrastructure for Astronomy. SPIE, Bellingham, p. 77401Z
Koenderink J., 1984, Biol. Cybern., 50, 363
Könyves V. et al., 2010, A&A, 518, L106
Lada C. J., Muench A. A., Rathborne J., Alves J. F., Lombardi M., 2008, ApJ, 672, 410
Lindeberg T., 1998, Int. J. Comput. Vis., 30, 79
Megeath S. T. et al., 2012, AJ, 144, 192
Men'shchikov A., André P., Didelon P., Motte F., Hennemann M., Schneider N., 2012, A&A, 542, A81
Molinari S., Schisano E., Faustini F., Pestalozzi M., di Giorgio A. M., Liu S., 2011, A&A, 530, A133

Motte F., André P., 2001, A&A, 365, 440
Muench A., Getman K., Hillenbrand L., Preibisch T., 2008, in Reipurth B., ed., Star Formation in the Orion Nebula I: Stellar Content. ASP Monograph Publications, San Francisco, p. 483
Nutter D., Ward-Thompson D., 2007, MNRAS, 374, 1413
Patil A., Huard D., Fonnesbeck C. J., 2010, J. Stat. Softw., 35, 1
Polychroni D. et al., 2013, ApJ, 777, L33
Reid M. A., Wilson C. D., 2005, ApJ, 625, 891
Salpeter E. E., 1955, ApJ, 121, 161
Schisano E. et al., 2014, ApJ, 791, 27
Schlafly E. F. et al., 2014, ApJ, 786, 29
Stutzki J., Bensch F., Heithausen A., Ossenkopf V., Zielinsky M., 1998, A&A, 336, 697
Takahashi S., Ho P. T. P., Teixeira P. S., Zapata L. A., Su Y.-N., 2013, ApJ, 763, 57
Verveer P. J., 2003–2005, SciPy: Open Source Scientific Tools for Python, scipy/ndimage/*. Available at: http://docs.scipy.org/doc/scipy-0.14.0/reference/generated/scipy.ndimage.measurements.label.html
Ward-Thompson D. et al., 2007, PASP, 119, 855
Witkin A. P., 1983, in Proc. 8th International Joint Conference on Artificial Intelligence (IJCAI'83), Volume 2, Morgan Kaufmann Publishers, San Francisco, CA, p. 1019
Wynn-Williams C. G., 1982, ARA&A, 20, 587

APPENDIX A: MULTISCALE HESSIAN-BASED MORPHOLOGICAL IDENTIFICATION

Image processing often requires the identification of isolated 'hill' or 'ridge' like structures in a topographical image representation. The simplest structures of this kind are the lowest order functions that contain local maxima in one or more of image dimensions. Structures such as these are very common in all areas of science and as a result have been the focus of image processing research for many years. The theoretical framework outlined below pioneered by Lindeberg (1998), Koenderink (1984) and Witkin (1983) was originally designed for the enhancement of vessel structures in medical imaging (Frangi et al. 1998), however, here we apply a generalized form of filtering for a variety of desired morphologies. Consider now a small portion of an image $g(x, y)$, for small values of x and

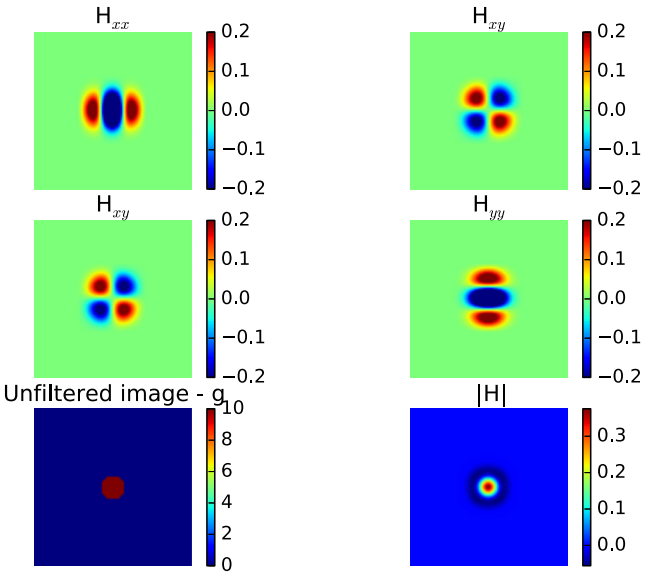

Figure A1. Hessian components and determinant response for a circular top-hat function of radius 3 pixels, at scale $\sigma = 6$ pixels. Note that the determinant peak response is much higher than that observed with the elongated object shown in the figure below.

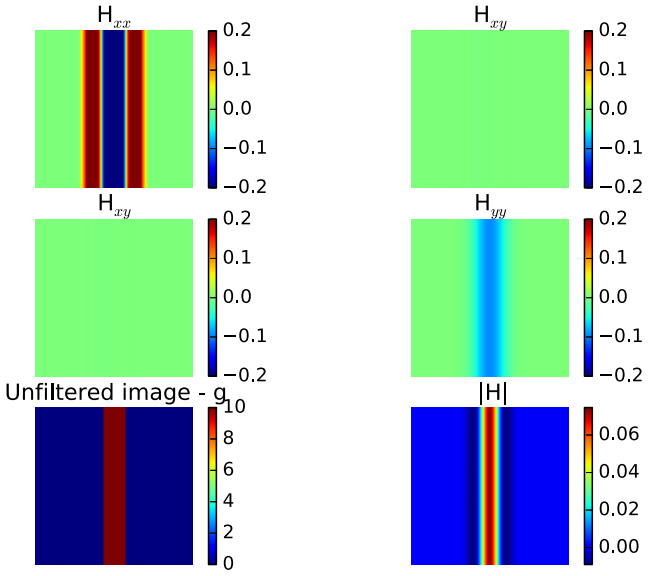

Figure A2. Hessian components and determinant response for a binary-ridge function of width 3 pixels, at scale $\sigma = 6$ pixels. Note that the magnitude of the Hessian response is only appreciable in the xx direction – resulting in a considerably decreased peak determinant response.

y from the centre of the portion, one may express the local features as a Maclaurin series to second order. The subscripts signify the directional derivative in the x or y directions:

$$g(x, y) \approx g(0, 0) + x g_x(0, 0) + y g_y(0, 0) + \frac{1}{2}\left(x^2 g_{xx}(0, 0) + 2xy g_{xy}(0, 0) + y^2 g_{yy}(0, 0)\right), \quad \text{(A1)}$$

or in matrix form:

$$g(x, y) \approx \frac{1}{2}\begin{bmatrix} x & y \end{bmatrix}\begin{bmatrix} \frac{\partial^2 g(x,y)}{\partial x^2} & \frac{\partial^2 g(x,y)}{\partial x \partial y} \\ \frac{\partial^2 g(x,y)}{\partial y \partial x} & \frac{\partial^2 g(x,y)}{\partial y^2} \end{bmatrix}\begin{bmatrix} x \\ y \end{bmatrix} + \begin{bmatrix} x \\ y \end{bmatrix}\begin{bmatrix} \frac{\partial g(x,y)}{\partial x} & \frac{\partial g(x,y)}{\partial y} \end{bmatrix} + g(0, 0), \quad \text{(A2)}$$

where

$$\mathbf{H} = \begin{pmatrix} \frac{\partial^2 g(x,y)}{\partial x^2} & \frac{\partial^2 g(x,y)}{\partial x \partial y} \\ \frac{\partial^2 g(x,y)}{\partial y \partial x} & \frac{\partial^2 g(x,y)}{\partial y^2} \end{pmatrix}. \quad \text{(A3)}$$

The matrix containing the second-order differentials is known as the Hessian, $\mathbf{H}$. This matrix contains most of the relevant information concerning hill/ridge-like structures and contains n^2 components for an n dimensional space. The components may be approximated by convolving the image with the second-order derivatives of a Gaussian distribution $G(x, y)$ of a given scale σ:

$$G(x, y) = \frac{1}{\sqrt{2\pi\sigma^2}} \exp\left(-\frac{(x^2 + y^2)}{2\sigma^2}\right) \quad \text{(A4)}$$

$$\mathbf{H}_{xx} \approx \sigma^\gamma \left(g(x, y) * \frac{1}{\sigma^2}\left(\frac{x^2}{\sigma^2} - 1\right) G(x, y)\right) \quad \text{(A5)}$$

$$\mathbf{H}_{yy} \approx \sigma^\gamma \left(g(x, y) * \frac{1}{\sigma^2}\left(\frac{y^2}{\sigma^2} - 1\right) G(x, y)\right) \quad \text{(A6)}$$

$$\mathbf{H}_{xy} \approx \sigma^\gamma \left(g(x, y) * \frac{xy}{\sigma^4} G(x, y)\right). \quad \text{(A7)}$$

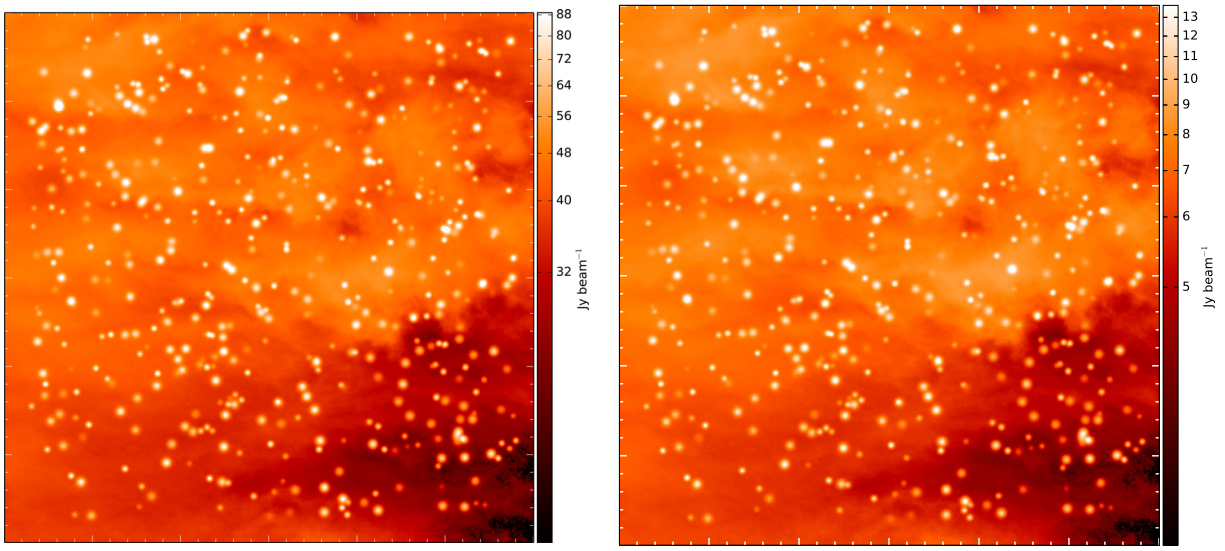

Figure B1. Fake 450 (left) and 850 μm (right) fields.

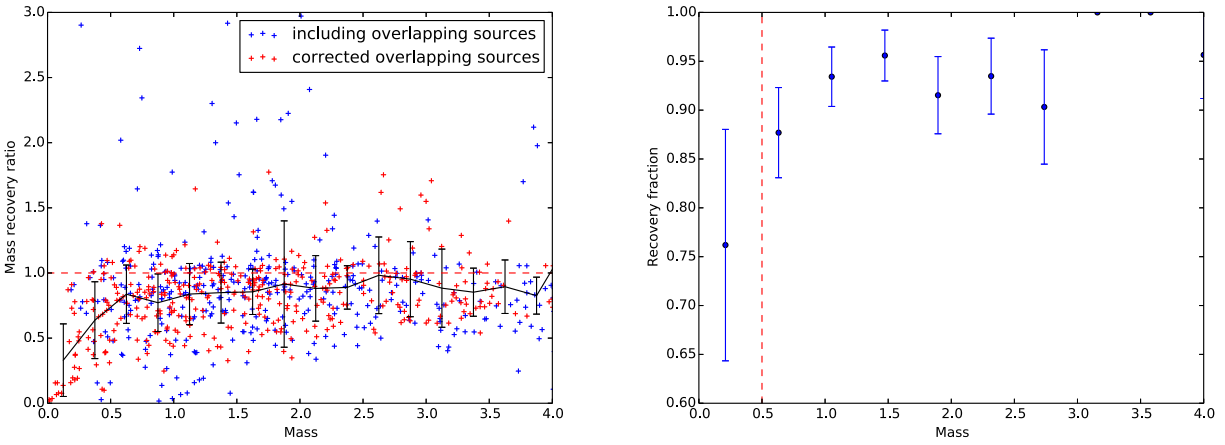

Figure B2. Left: mass recovery ratio as a function of true mass. The red crosses represent the lowest mass recovery ratio for instances in which multiple input core locations overlap with a single recovered core, demonstrating the effects of source confusion on mass recovery. The blue crosses indicate the same recovery ratios without correcting for overlapping sources. Right: fraction of cores recovered as a function of mass. Note the >85 per cent recovery for masses >0.5 $M_{\odot}$. The error bars shown are Poisson 'counting' errors, i.e $\sqrt{N}$.

In addition to the varying σ value, one may vary the value of γ to emphasize small or large-scale features with $\gamma = 1$ giving uniform enhancement across all scales. Once the Hessian components have been generated, there are a variety of methods one may use to highlight their desired structures according to morphology, however, this particular investigation requires only the enhancement of relatively circular, compact structure of a given scale. An ideal identification method for this description of structure is the Hessian determinant. The Hessian determinant of a circular object with diameter matching the scale value σ will be larger than the corresponding Hessian determinant of an elongated structure as an elongated structure at any orientation will lack the amplitude of response from the second-order derivative filter in the direction parallel to the structure's longitudinal axis. As a result, an object will be preferentially enhanced based upon its radial symmetry at a given scale. This effect is illustrated in Figs A1 and A2.

APPENDIX B: COMPLETENESS TESTING

Due to the novel nature of the Hessian determinant algorithm and its application to SCUBA-2 data, we simulate 450 and 850 μm observations of compact sources in order to assess the reliability of the recovered mass function. 500 randomly positioned Gaussian sources with the following properties were injected into 1° × 1° (with 6 arcsec pixels) fields representing the 450 and 850 μm core emission detected by SCUBA-2.

(i) σ ranging between 12 and 24 arcsec or FWHM ranging between 0.06 and 0.12 pc at a radial distance of 450 pc.

(ii) 450 μm intensities ranging between 0 and 90 Jy beam^{-1} (at the diluted 850 μm resolution), consistent with the typical core intensities observed in Orion A North.

(iii) 450 to 850 μm intensity ratios ranging between 6 and 8 to simulate a variety of temperatures, with masses ranging between 0 and 10 $M_{\odot}$.

As each source was injected, the mass and peak location was stored for comparison to the recovered cores. Following the source injection, we add a diffuse cloud-like 12 K background with 450 μm intensities ranging between 25 and 55 Jy beam^{-1} (see Fig. B1). This fluctuating background is sourced from an image of terrestrial cloud formations which has a Fourier power spectrum quantitatively similar to that of molecular clouds $|F(k)|^2 \propto k^{-\beta}$ where $\beta \approx 3$ (Stutzki

et al. 1998). Additionally, we also insert Gaussian noise at a level equal to the thermal noise in the SCUBA-2 bolometer signals given in Section 2. The temperature and column density maps were generated in an identical manner to that outlined in Section 3. The Hessian determinant source extraction algorithm is then applied to the column density data (with identical scale sensitivity to that used on Orion A North) to recover the mass function. The true (input) core peak locations were compared with the extracted core position (calculated by averaging the coordinates within the core boundary). If a core location was recovered within 3 pixels $\equiv$ 18 arcsec of an input core peak location, the core was deemed 'recovered' and the input to recovered mass ratio was stored. The plot shown in Fig. B2 (left) demonstrates a consistent mass recovery of $\sim$90 per cent of the input mass, suggesting that the detected core boundary consistently extends to the 1σ radius of the input source. Fig. B2 (right) demonstrates that for masses exceeding $\sim$0.5 $M_{\odot}$, the recovery function flattens out and exceeds 85 per cent. Consequently, we assume a 85 per cent completeness limit for masses exceeding 0.5 $M_{\odot}$.

SUPPORTING INFORMATION

Additional Supporting Information may be found in the online version of this article:

(http://mnras.oxfordjournals.org/lookup/suppl/doi:10.1093/mnras/stu2297/-/DC1).

Please note: Oxford University Press are not responsible for the content or functionality of any supporting materials supplied by the authors. Any queries (other than missing material) should be directed to the corresponding author for the article.

[1]*Astrophysics Group, Cavendish Laboratory, J J Thomson Avenue, Cambridge CB3 0HE, UK*
[2]*Kavli Institute for Cosmology, Institute of Astronomy, University of Cambridge, Madingley Road, Cambridge CB3 0HA, UK*
[3]*Physics and Astronomy, University of Exeter, Stocker Road, Exeter EX4 4QL, UK*
[4]*NRC Herzberg Astronomy and Astrophysics, 5071 West Saanich Rd, Victoria, BC V9E 2E7, Canada*
[5]*Department of Physics and Astronomy, University of Waterloo, Waterloo, ON N2L 3G1, Canada Â*
[6]*Joint Astronomy Centre, 660 N. A'ohōkū Place, University Park, Hilo, Hawaii 96720, USA*
[7]*Department of Physics and Astronomy, University of Victoria, Victoria, BC V8P 1A1, Canada*
[8]*Department of Astronomy, Cornell University, Ithaca, NY 14853, USA*
[9]*Leiden Observatory, Leiden University, PO Box 9513, NL-2300 RA Leiden, The Netherlands*
[10]*School of Physics and Astronomy, Cardiff University, The Parade, Cardiff CF24 3AA, UK*
[11]*Jeremiah Horrocks Institute, University of Central Lancashire, Preston, Lancashire PR1 2HE, UK*
[12]*European Southern Observatory (ESO), D-85748 Garching, Germany*
[13]*Jodrell Bank Centre for Astrophysics, Alan Turing Building, School of Physics and Astronomy, University of Manchester, Oxford Road, Manchester M13 9PL, UK*
[14]*Centre de Recherche en Astrophysique du Québec et département de physique, Université de Montréal, C.P. 6128, succ. centre-ville, Montréal, QC H3C 3J7, Canada*
[15]*James Madison University, Harrisonburg, Virginia 22807, USA*
[16]*School of Physics, Astronomy & Mathematics, University of Hertfordshire, College Lane, Hatfield, Hertfordshire AL10 9AB, UK*
[17]*Astrophysics Research Institute, Liverpool John Moores University, Egerton Warf, Birkenhead CH41 1LD, UK*
[18]*Imperial College London, Blackett Laboratory, Prince Consort Rd, London SW7 2BB, UK*
[19]*Department of Physics & Astronomy, University of Manitoba, Winnipeg, MB R3T 2N2 Canada*
[20]*Dunlap Institute for Astronomy & Astrophysics, University of Toronto, 50 St George St, Toronto, ON M5S 3H4 Canada*
[21]*Physics & Astronomy, University of St Andrews, North Haugh, St Andrews, Fife KY16 9SS, UK*
[22]*Department of Physical Sciences, The Open University, Milton Keynes MK7 6AA, UK*
[23]*The Rutherford Appleton Laboratory, Chilton, Didcot OX11 0NL, UK*
[24]*UK Astronomy Technology Centre, Royal Observatory, Blackford Hill, Edinburgh EH9 3HJ, UK*
[25]*Institute for Astronomy, Royal Observatory, University of Edinburgh, Blackford Hill, Edinburgh EH9 3HJ, UK*
[26]*Centre de recherche en astrophysique du Québec et Département de physique, de génie physique et d'optique, Université Laval, 1045 avenue de la médecine, QC G1V 0A6, Canada*
[27]*Department of Physics and Astronomy, UCL, Gower St, London WC1E 6BT, UK*
[28]*Department of Physics and Astronomy, McMaster University, Hamilton, ON L8S 4M1, Canada*
[29]*Department of Physics, University of Alberta, Edmonton, AB T6G 2E1, Canada*
[30]*Max Planck Institute for Astronomy, Königstuhl 17, D-69117 Heidelberg, Germany*
[31]*University of Western Sydney, Locked Bag 1797, Penrith NSW 2751, Australia*
[32]*National Astronomical Observatory of China, 20A Datun Road, Chaoyang District, Beijing 100012, China*

This paper has been typeset from a TEX/LATEX file prepared by the author.